ChemComm

COMMUNICATION

View Article Online
View Journal | View Issue

Cite this: *Chem. Commun.*, 2024, **60**, 13959

Received 5th October 2024,
Accepted 1st November 2024

DOI: 10.1039/d4cc05220j

rsc.li/chemcomm

Controlled nucleation of ultrasmall MoO_3 nanoparticles on defective graphene for enhanced ammonia efficiency†

Sakshi Bhardwaj, Sumon Santra and Ramendra Sundar Dey *

Ultrasmall nanoparticles on nanocarbons enhance the electrocatalytic nitrogen reduction (NRR) efficiency. Herein, we demonstrate a novel method for depositing MoO_3 nanoparticles on defective graphene, achieving a high faradaic efficiency (FE) of 43.1% at −0.2 V *vs.* RHE.

Ammonia (NH_3), the second most-produced chemical globally, plays a critical role in the agriculture industry and serves as a carbon-free energy carrier.[1] Recently, the electrochemical nitrogen reduction reaction (NRR) has garnered significant attention due to its potential to leverage renewable energy sources and operate under ambient conditions, contrasting with the energy-intensive Haber–Bosch process.[2] However, despite several advantages, the electrocatalytic NRR faces two primary challenges: (1) the high overpotential required to break the strong triple bond in N_2 molecules and (2) the competitive hydrogen evolution reaction (HER) in aqueous electrolytes.[3] To achieve efficient NH_3 production, electrocatalysts must be engineered to effectively adsorb, activate, and reduce N_2 molecules with high selectivity and stability.

Several electrocatalysts including noble metals[4,5] as well as non-noble metal-based electrocatalysts such as V, Mo, Ni and Fe[6–9] have been developed in the past for efficient NH_3 synthesis. Metal-free catalysts, especially B-based materials, are being explored widely due to their high tendency for N_2 adsorption.[10] Recently, Mo-based electrocatalysts have gained significant attention due to their similar d-electron structure to that of Pt.[11] In biological nitrogen fixation, Mo serves as a key cofactor in nitrogenase enzymes.[12] Inspired by nature, Mo-based catalysts have been extensively designed for the development of electrocatalytic nitrogen fixation, demonstrating robustness and stability.[13–15] Furthermore, theoretical studies support the potential of Mo-based electrocatalysts for the NRR.[16] It is important to note that the size and distribution of metal nanoparticles on graphene or other conductive supports are crucial factors influencing electrocatalytic activity. Small, well-dispersed nanoparticles provide a greater number of active sites, enhancing catalytic performance.

In this work, we employed a simple ultrasonic method to deposit MoO_3 nanoparticles onto defective graphene sheets. By conducting the process under ice-cold conditions (0 °C), we were able to control the nucleation rate, leading to the formation of ultrasmall nanoparticles on defective graphene (Mo-DG). This strategy significantly enhances the exposure of active sites to N_2 molecules, resulting in a high faradaic efficiency (FE) of 43.1% at −0.2 V *vs.* RHE. The reaction intermediates were analyzed using *in situ* ATR-IR and Raman spectroscopy, providing insight into the reaction mechanism. This work presents a promising catalyst design strategy for the sustainable production of ammonia.

Fig. 1a schematically illustrates the synthesis of the Mo-DG catalyst, while the experimental details are provided in the ESI.† Briefly, this was a two-step synthesis process where the first step was the synthesis of N-doped defective graphene (DG) prepared using our previously reported method.[17] The second step was decorating DG with ultrasmall MoO_3 nanoparticles

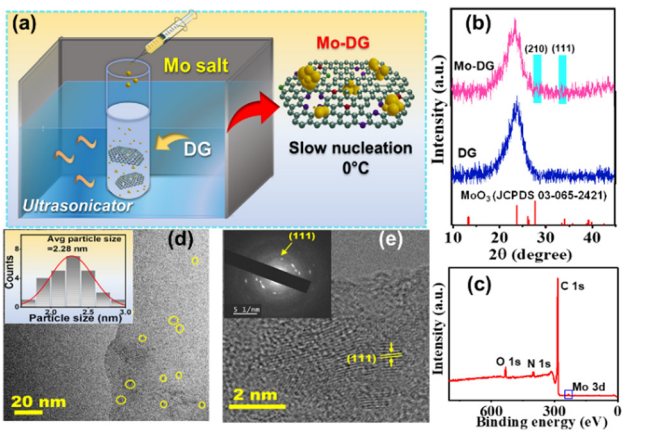

Fig. 1 (a) Schematic illustration of the synthesis of Mo-DG; (b) XRD pattern of DG, Mo-DG and JCPDS of MoO_3; (c) XPS survey spectra of Mo-DG; (d) and (e) HRTEM images of Mo-DG; inset of (d) particle size distribution plot of Mo-DG; inset of (e) SAED of the inset of Mo-DG.

Institute of Nano Science and Technology, Sector-81, Mohali-140306, Punjab, India. E-mail: rsdey@inst.ac.in

† Electronic supplementary information (ESI) available. See DOI: https://doi.org/10.1039/d4cc05220j

(Mo-DG) under ice-cold conditions in an ultrasonicator to control the nucleation rate. Also, the same sample was prepared at room temperature (Mo-DG RT) as temperature plays an important role in this process. Under ice-cold conditions, this nucleation process is slowed down. At defect sites in carbon materials, ultrasonication caused MoO_3 to get deposited by the charge redistribution of carbon atoms. The oxidation of Mo occurred by the solution of dissolved oxygen. Then, these metal sites act as active centres for electrocatalytic reactions. In addition to the lower temperature range, the ultrasound-assisted synthesis also ensured uniformity. We did an inductively coupled plasma mass spectrometric (ICP-MS) study which showed that Mo-DG RT had a higher content of Mo (2.5%) as compared to Mo-DG (0.9%) synthesized under the same conditions except for temperature difference.

The XRD pattern of DG, Mo-DG RT, and Mo-DG displayed a renowned peak of graphene at $2\theta = 23.6^\circ$. Additionally, in Mo-DG and Mo-DG RT, two peaks at 27.5° and 33.8° were observed ascribed to the (210) and (111) planes of MoO_3 (MoO_3, JCPDS 03-065-2421) (Fig. 1b and Fig. S1, ESI†).[18] The presence of defects in the carbon framework gives rise to irregularity, which can be observed by Raman spectroscopy. The two peaks at 1350 and 1580 cm^{-1} were responsible for the D-band and G-bands in the carbon[19] (Fig. S2 in ESI†). The chemical composition and the surface chemical state of the Mo-DG catalyst were determined by X-ray photoelectron spectroscopy (XPS). The full survey spectra of all the samples identified the presence of their corresponding elements (C, N, O, Mo), as shown in Fig. 1c. The deconvoluted XPS spectra of Mo 3d (Fig. S3a in ESI†) showed two well-separated and distinct peaks corresponding to Mo^{6+} ($3d_{5/2}$ and Mo $3d_{3/2}$ obtained at 232.8 eV and 235.7 eV, respectively).[20] The O 1s spectra (Fig. S3b in ESI†) consisted of 531.6 and 533.6 eV peaks responsible for C═O and C–O. Moreover, a merged peak at 530.3 eV was indexed to the Mo–O bond, confirming the Mo–O coordination. The C 1s spectrum was deconvoluted into three peaks: 284.5, 285.6, and 286.7 eV corresponding to C═C, C–N/C–O, and C═O, respectively (Fig. S4 in ESI†). The narrow N 1s spectra were deconvoluted into four peaks, demonstrating the presence of pyridinic, pyrrolic, graphitic, and oxidized-N centered at 397.8, 400.89, 401.9, and 404.5 eV, respectively (Fig. S5, ESI†). The morphology of Mo-DG was primarily studied by field emission scanning electron microscope (FESEM). Fig. S6(a) and (b) in the ESI† depict the interconnected porous graphene sheets, which can be attributed to its high surface area having a number of active sites that enable efficient mass transport for the NRR. Furthermore, the transmission electron microscopy (TEM) image (Fig. S7, ESI†) showed wrinkled graphene sheets. The MoO_3-nanoparticles were encircled with yellow color in high-resolution TEM ((HRTEM), Fig. 1d). The particle size distribution plot (inset: Fig. 1d) confirmed the formation of ultrasmall nanoparticles (average size 2.28 nm). However, the TEM and HRTEM images of Mo-DG RT (Fig. S8(a) and (b), ESI†) illustrated the formation of nanoparticles in the range of 10–15 nm, which showed the temperature dependency of the synthesis process. Fig. 1e displays identifiable lattice fringes with spacings of 0.26 nm corresponding to the (111) plane as obtained in the selected area electron diffraction (SAED) image (inset: Fig. 1e). Furthermore, the presence of C, N, O, and Mo over the graphene sheets was revealed by energy-dispersive X-ray spectroscopy (EDS) and TEM mapping (Fig. S9 and S10, ESI†). These characterizations corroborated the formation of ultrasmall nanoparticles of MoO_3 on defective graphene sheets.

Being biologically inspired by the nitrogenase enzyme for nitrogen fixation, we evaluated the electrocatalytic NRR activity of Mo-DG using an H-cell. Firstly, the purity of N_2 feeding gas was checked using gas chromatography (Fig. S11, ESI†), confirming that N_2 was pure. Additionally, the N_2 gas was passed through acid and base trap solutions to check for any interference of extra ammonia. Other NO_x impurities were also checked spectrophotometrically. The generated NH_3 in each experiment was measured spectrophotometrically using the indophenol blue method,[21] relying on a calibration curve created from known NH_3 concentrations (Fig. S12 and S13, ESI†). This procedure was similarly applied to acid, base trap solutions, and NO_x to assess the purity of N_2 (Fig. S14–S19, ESI†). For the acid, base trap, and NO_x detection, no absorbance was recorded under the UV-visible spectrophotometer (Fig. S20 and S21, ESI†). In the NRR, first, N_2 molecules are adsorbed over the electrocatalyst followed by their hydrogenation to produce ammonia. Typically, in aqueous electrolytes, the electrocatalyst is more likely to undergo the HER rather than the NRR due to the abundance of protons. To assess the selectivity of Mo-DG, cyclic voltammetry (CV) experiments were conducted in Ar and N_2 environments at varying scan rates in the non-faradaic region (Fig. S22(a) and (b), ESI†). Linear regression analysis was then performed to establish a correlation between scan rate and Δj (the difference between anodic and cathodic current densities) derived from the CV curves, producing a straight line with a slope corresponding to the double-layer capacitance (C_{dl}) value (Fig. S22c, ESI†). The electrochemically active surface area (ECSA) is directly proportional to C_{dl}, revealing a lower ECSA in the presence of N_2 compared to Ar (Fig. S22d, ESI†). This outcome suggested that a greater number of N_2 molecules were adsorbed on the Mo-DG surface, thus favoring N_2 adsorption, which is the initial step in the NRR. In our material Mo-DG, Mo acted as the active center due to its facile coordination chemistry with N_2 molecules and their intermediates, promoting an efficient NRR pathway.[22] Following this, we conducted linear sweep voltammetry (LSV) in Ar and N_2-saturated 0.5 M Na_2SO_4 at a scan rate of 10 mV s^{-1} to determine the activity of Mo-DG in the NRR (Fig. 2a). The increased current density and positive shift of onset potential in LSV in N_2 medium indicated the NRR activity of Mo-DG. LSV suggested the potential region (−0.1 to −0.5 V *vs.* RHE) to be investigated further in a chronoamperometric (CA) study to find the yield and faradaic efficiency (FE) of the catalyst during the NRR (Fig. S23, ESI†). The UV-vis spectra of all the catholytes were tested (Fig. S24, ESI†) by the indophenol blue method to determine the FE and yield of ammonia. The highest FE of 43.1% with a maximum NH_3 yield of 28.4 μg h^{-1} mg_{cat}^{-1} was attained at −0.2 V *vs.* presented in the bar plot of Fig. 2b. Our

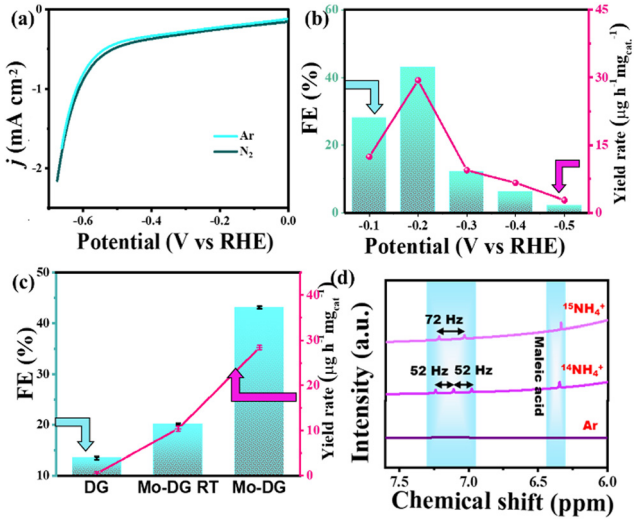

Fig. 2 (a) LSV curves of Mo-DG in Ar and N_2 saturated 0.5 M Na_2SO_4 with scan rate 10 mV s^{-1}, (b) the bar plot of FE and NH_3 yield rate for Mo-DG at different potentials, (c) FE and NH_3 yield rate for DG, Mo-DG-RT, and Mo-DG at −0.2 V *vs.* RHE, (d) isotope labeling experiment displaying ^1H NMR spectra obtained after NRR in 0.5 M Na_2SO_4 with Ar, $^{14}N_2$ and $^{15}N_2$ as feeding gases.

electrocatalyst demonstrated selectivity towards NH_3 production as no side product, hydrazine (N_2H_4), was obtained as indicated by its calibration curve (Fig. S25 and S26, ESI†) and the UV plot determined by the Watt and Chrisp method (Fig. S27, ESI†). The effect of ultrasmall nanoparticles of MoO_3 in Mo-DG was confirmed by the comparative NRR study of DG and Mo-DG RT (Fig. S28, ESI†) concluded in the form of a bar plot (Fig. 2c). The high FE can be attributed to the presence of Mo active sites that facilitate the adsorption and reduction of N_2 molecules. Table S1 (ESI†) shows its excellent performance in comparison to available literature studies. Moreover, few control experiments were conducted to confirm that ammonia production was indeed from the catalyst. CA runs were carried out in an Ar-purged environment, at open-circuit potential (OCP) in N_2 conditions, at −0.2 V. The results (Fig. S29 and S30, ESI†) confirmed that Mo-DG was solely responsible for NH_3 production. Furthermore, the stability of Mo-DG was assessed for long-term usage, and it remained stable for up to 15 h with no change in current density (Fig. S31, ESI†). The FE% obtained after 2 h and 15 h was almost similar, confirming the stability of the material (inset: Fig. S31 in ESI†). Next, to examine the durability of the electrocatalyst Mo-DG, its cyclability was checked for five cycles of one hour (Fig. S32, ESI†) demonstrating that the UV-vis spectra remained consistent throughout the experiment (Fig. S33, ESI†), leading to reproducible FE and ammonia yield, as shown in Fig. S34 (ESI†). This compelling experiment provided evidence for the durability and resilience of the Mo-DG. To confirm that the ammonia produced originated from the supplied nitrogen gas, $^{15}N_2$ isotope labeling experiments were conducted. As anticipated, no peak was observed in the Ar medium while a triplet was detected in ^1H-NMR when $^{14}N_2$ gas was purged and a doublet was observed indicating the formation of $^{15}NH_4^+$ with $^{15}N_2$ as purged gas (Fig. 2d). This confirmed that the ammonia production was solely from the purged gas. Additionally, to verify the FE and yield, the amount of ammonia was quantified using NMR analysis with the assistance of maleic acid, following eqn (S4) in the ESI.† The FE calculated through two different methods – UV-spectroscopy and NMR analysis – showed close agreement, validating the accuracy of the measurements.

Furthermore, to study the kinetics of the NRR we did a rotating ring disc electrode (RRDE) experiment (Fig. 3a) which is a fast and qualitative tool for ammonia detection. Electrochemical ammonia production involves a six-electron-proton process where N_2 gas diffuses from the electrolyte to the catalyst, forming an electrode–electrolyte interface where the reaction occurs. In this setup, the nitrogen will be reduced on the ring part of the electrode having Mo-DG as an electrocatalyst, while the NH_3 produced is detected by its conversion to NO_x on the Pt ring of RRDE. LSV was performed on RRDE with a rotation speed of 1600 rpm (Fig. 3b). The rotation helped to push N_2 molecules toward the electrode surface, facilitating the NRR on the disc part of the RRDE. Additionally, Fig. 3b shows that Mo-DG achieved better onset current density (0.34 mA cm^{-2}) and onset potential (−0.5 V *vs.* RHE) as compared to DG due to NRR occurring across the electrode–electrolyte interface. The N_2 reduction to ammonia can further be verified by its oxidation to NO_x species occurring on the Pt ring of the RRDE, with an oxidation peak observed at 0.73 V. CV was conducted to detect this irreversible oxidation peak of ammonia, confirming ammonia synthesis by N_2 electroreduction (Fig. 3c). No peak was observed at 0.2 V, which rules out the presence of the N_2H_4 oxidation product. This further proves the selectivity of Mo-DG. The mechanism followed in the NRR is shown in Fig. 3d. The transition metal Mo acts as the active centre in Mo-DG. The empty d-orbitals of Mo can accept the

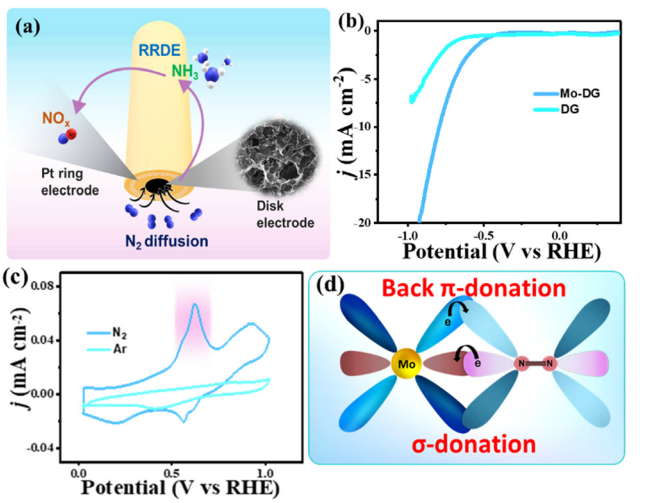

Fig. 3 (a) Schematic representation of the NRR taking place on the RRDE setup; (b) LSV of different catalysts at 2 mV s^{-1} N_2 atmosphere on the RRDE; (c) CV performed at scan rate 10 mV s^{-1} representing the ammonia oxidation on the Pt ring of the RRDE electrode after the NRR; (d) reaction mechanism followed by Mo-DG during the NRR.

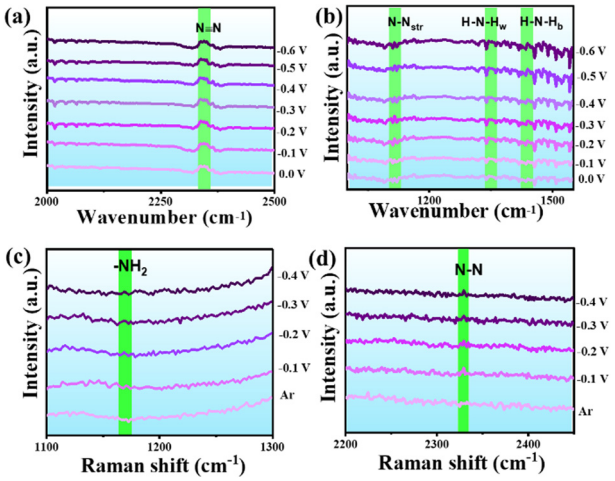

Fig. 4 (a) and (b) *In situ* ATR-IR data of Mo-DG; (c) and (d) *in situ* Raman data of Mo-DG.

electrons from the N_2 molecule (σ-donation). Also, the filled d-orbitals of Mo can provide electrons to the π* antibonding orbital of N_2. This interplay of acceptance and donation of electrons between Mo and N_2 molecules activates and consequently, reduces them.

For determining the intermediates in the NRR process an *in situ* attenuated total reflectance-Fourier transform infrared (ATR-FTIR) spectroscopic study was conducted on the synthesized Mo-DG using a setup, as shown in Fig. S35 (ESI†). The nitrogen molecule is IR inactive due to its non-polarity. Although a stretching frequency of N_2 around 2335 cm^{-1} was observed in its spectrum during the electrochemical NRR due to alteration in its charge polarity. This frequency was absent in the Ar medium or at open circuit potential (OCP) in the N_2 medium, as shown in Fig. S36a (ESI†). When a potential was applied ranging from 0 to −0.6 V *vs.* RHE in an N_2 atmosphere, this peak remained detectable, as illustrated in Fig. 4a. Additionally, three peaks at 1109, 1340, and 1447 cm^{-1} were observed during the NRR, corresponding to $N–N_{stretching}$, $–NH_{2wagging}$, and $H–N–H_{bending}$ vibrations, respectively.[23] These peaks confirmed the formation of intermediates during the NRR, which were not seen with Ar or OCP, as shown in Fig. 4b and Fig. S36b (ESI†). These vibrational bands indicated the presence of N_2H_y ($2 \leq y \leq 4$) intermediates on the catalyst surface and the electrolyte interface during the electrochemical NRR. It implies that NRR follows the associative mechanism on the catalyst surface, as shown in Fig. S37 in the ESI.† This conclusion is quite logical, as breaking the N≡N triple bond at room temperature is challenging without introducing hydrogen atoms. Moreover, an *in situ* Raman experiment was carried out in Ar and N_2 saturated electrolyte. Two peaks located at 1152 and 2333 cm^{-1}, corresponding to $–NH_2$ and N–N,[24,25] respectively, were observed (Fig. 4c and d), which were absent in the case of Ar. A band representing $–NH_{str}$ was observed between 3200–3300 cm^{-1} (Fig. S38, ESI†).[26] These two *in situ* characterizations confirm the formation of different intermediates during the NRR.

In summary, the controlled nucleation of ultrasmall nanoparticles of MoO_3 on defective graphene under ice-cold conditions led to efficient NRR by achieving an excellent FE of 43.1% at −0.2 V *vs.* RHE. The kinetics were studied using RRDE. Furthermore, *in situ* ATR-IR and Raman studies were done to determine the reaction intermediates. This study can be further extended to explore field catalyst design for efficient NH_3 generation.

The authors acknowledge BRNS (58/14/19/2023-BRNS) for financial support.

Data availability

The data supporting this article have been included as part of the ESI.†

Conflicts of interest

There are no conflicts to declare.

References

1 C. Smith, A. K. Hill and L. Torrente-Murciano, *Energy Environ. Sci.*, 2020, **13**, 331–344.
2 J. Humphreys, R. Lan and S. Tao, *Adv. Energy Sustainable Res.*, 2021, **2**, 2000043.
3 C. Tang and S. Z. Qiao, *Chem. Soc. Rev.*, 2019, **48**, 3166–3180.
4 M. Nazemi, S. R. Panikkanvalappil and M. A. El-Sayed, *Nano Energy*, 2018, **49**, 316–323.
5 Z. Geng, Y. Liu, X. Kong, P. Li, K. Li, Z. Liu, J. Du, M. Shu, R. Si, J. Zeng, Z. Geng, Y. Liu, X. Kong, P. Li, K. Li, Z. Liu, J. Du, J. Zeng, M. Shu and R. Si, *Adv. Mater.*, 2018, **30**, 1803498.
6 H. Cheng, L.-X. Ding, G.-F. Chen, L. Zhang, J. Xue, H. Wang, H. Cheng, L. Ding, G. Chen, L. Zhang, J. Xue and H. Wang, *Adv. Mater.*, 2018, **30**, 1803694.
7 H. Yang, W. Zou, K. Ken Ostrikov, C. Zhang and A. Du, *Appl. Surf. Sci.*, 2023, **640**, 158277.
8 Y. Wang, X. Cui, J. Zhao, G. Jia, L. Gu, Q. Zhang, L. Meng, Z. Shi, L. Zheng, C. Wang, Z. Zhang and W. Zheng, *ACS Catal.*, 2019, **9**, 336–344.
9 J. Wu and Y. X. Yu, *J. Phys. Chem. C*, 2022, **126**, 12460–12471.
10 J. Wu and Y. X. Yu, *J. Phys. Chem. C*, 2021, **125**, 23699–23708.
11 R. Ge, J. Huo, M. Sun, M. Zhu, Y. Li, S. Chou and W. Li, *Small*, 2021, **17**, 1903380.
12 O. Einsle and D. C. Rees, *Chem. Rev.*, 2020, **120**, 4969–5004.
13 H. Cheng, L.-X. Ding, G.-F. Chen, L. Zhang, J. Xue, H. Wang, H. Cheng, L. Ding, G. Chen, L. Zhang, J. Xue and H. Wang, *Adv. Mater.*, 2018, **30**, 1803694.
14 L. Han, X. Liu, J. Chen, R. Lin, H. Liu, F. Lü, S. Bak, Z. Liang, S. Zhao, E. Stavitski, J. Luo, R. R. Adzic and H. L. Xin, *Angew. Chem.*, 2019, **131**, 2343–2347.
15 R. Akter, S. S. Shah, M. A. Ehsan, M. N. Shaikh, M. H. Zahir, M. A. Aziz and A. J. S. Ahammad, *Chem. – Asian J.*, 2024, **19**, e202300797.
16 C. Ling, X. Bai, Y. Ouyang, A. Du and J. Wang, *J. Phys. Chem. C*, 2018, **122**, 16842–16847.
17 S. Bhardwaj, S. Kapse, S. Dan, R. Thapa and R. S. Dey, *J. Mater. Chem. A*, 2023, **11**, 17045–17055.
18 S. Wang, N. Liu, J. Rao, Y. Yue, K. Gao, J. Su, L. Li, X. Jiang, Z. Liu and Y. Gao, *J. Mater. Chem. A*, 2017, **5**, 22199–22207.
19 Y. Jia, L. Zhang, A. Du, G. Gao, J. Chen, X. Yan, C. L. Brown and X. Yao, *Adv. Mater.*, 2016, **28**, 9532–9538.
20 Á. Arnosa-Prieto, M. A. González-Gómez, P. García-Acevedo, L. de Castro-Alves, Y. Piñeiro and J. Rivas, *Mater. Today Chem.*, 2024, **35**, 101854.
21 S. Bhardwaj, S. K. Das, A. Biswas, S. Kapse, R. Thapa and R. S. Dey, *Chem. Sci.*, 2023, **14**, 8936–8945.
22 Y. Yang, S. Feng, J. Su, Y. Gong and J. Wang, *ACS Sustainable Chem. Eng.*, 2022, **10**, 14064–14072.
23 Y. Yao, S. Zhu, H. Wang, H. Li and M. Shao, *J. Am. Chem. Soc.*, 2018, **140**, 1496–1501.
24 M. Wang, S. Liu, H. Ji, T. Yang, T. Qian and C. Yan, *Nat. Commun.*, 2021, **12**, 1–10.
25 H. Ohno, Y. Iizuka and S. Fujita, *J. Glaciol.*, 2021, **67**, 903–908.
26 M. Lozinšek, *Acta Chim. Slov.*, 2015, **62**, 378–384.

